American Mineralogist, Volume 106, pages 1668–1678, 2021

High-temperature and high-pressure Raman spectra of $Fo_{89}Fa_{11}$ and $Fo_{58}Fa_{42}$ olivines: Iron effect on thermodynamic properties

Dan Liu[1], Xinzhuan Guo[2], Joseph R. Smyth[3], Xiang Wang[1], Xi Zhu[1], Yunfan Miao[1], Jiayuan Bai[1], and Yu Ye[1,*]

[1]State Key Laboratory of Geological Processes and Mineral Resources, China University of Geosciences, Wuhan 430074, China
[2]Key Laboratory for High-Temperature and High-Pressure Study of the Earth's Interior, Institute of Geochemistry, Chinese Academy of Sciences, Guiyang 550081, China
[3]Department of Geological Sciences, University of Colorado, Boulder, Colorado 80309, U.S.A.

Abstract

The intrinsic anharmonicity plays an important role in the thermodynamic properties of minerals at the high-temperature conditions of the mantle. To investigate the effect of iron on the thermodynamic properties of olivine, the most abundant mineral in the upper mantle, we collected in situ high-temperature and high-pressure Raman spectra of natural $Fo_{89}Fa_{11}$ and synthetic $Fo_{58}Fa_{42}$ samples. $Fo_{58}Fa_{42}$ dissociates to enstatite + quartz + Fe_2O_3(+Fe) at 893 K. All the Raman-active modes systematically shift to lower frequencies at elevated temperatures, whereas to higher frequencies with increasing pressure. The A_g mode at ~960 cm^{-1} is more sensitive to the variations of temperature and pressure than other internal modes. The crystal-field splitting of the vibrational energy states becomes slightly weakened at high temperatures but strengthened at elevated pressures. We calculated the isobaric (γ_{iP}) and isothermal (γ_{iT}) mode Grüneisen parameters for these olivine samples. The intrinsic anharmonic parameters (a_i) are negative for both the lattice and internal vibrations, and our calculations indicate that the intrinsic anharmonicity makes positive contributions to the thermodynamic properties of olivine at high temperatures, such as the internal energy (U), heat capacities (C_V and C_P), and entropy (S). Iron incorporation further increases the magnitudes of these anharmonic contributions. In addition, the Fe effect on the intrinsic anharmonicity may also apply to other thermodynamic properties in olivine, such as equations of state and equilibrium isotopic fractionations, which are important in constraining physical and chemical properties of the upper mantle.

Keywords: Olivine, in situ high-temperature Raman, high-pressure Raman, Grüneisen parameter, intrinsic anharmonicity, thermodynamic properties

Introduction

The harmonic (or quasi-harmonic) approximation, such as the Debye model, traditionally plays a central role in modeling thermodynamic properties of minerals, such as heat capacities (Cynn et al. 1996; Holland and Powell 1998), equations of state (Oganov and Dorogokupets 2003), and equilibrium isotopic fractionation factors (Horita et al. 2002; Wu et al. 2015). In this approximation, the movement of atoms inside the lattice structure is simplified as harmonic vibrations, which can deviate from reality, especially at high temperatures. Then, the intrinsic anharmonic correction becomes necessary to restore agreement between theoretical models and experiments (observations) (e.g., Gillet et al. 1991; Polyakov 1998; Dorogokupets and Oganov 2004; Wu 2015; Liu et al. 2019a; Zhu et al. 2019).

Gillet et al. (1991, 1997) evaluated the anharmonic contribution to the heat capacities of anhydrous forsterite (Mg-end-member olivine) by in situ Raman spectra measured at high pressures and temperatures. On the basis of the temperature and pressure dependences of the vibrational frequencies, Gillet (1991) derived the isobaric and isothermal mode Grüneisen parameters as well as the intrinsic anharmonic parameters. Next, the heat capacities were computed according to the vibrational frequency models proposed by Kieffer (1979) and Hofmeister (1987), and the anharmonic contribution to the heat capacities reached a percentage of 6~7% when extrapolated to 2000 K, with respect to the harmonic approximation. Furthermore, Yang et al. (2015) and Liu et al. (2019b) investigated the intrinsic anharmonicity in hydrous forsterite samples since olivine can contain a significant amount of structural water (as hydroxyl groups), up to a few thousand parts per million by weight under the upper mantle condition (e.g., Kohlstedt et al. 1996; Smyth et al. 2006). The calculation revealed that hydration would further increase the magnitude of the anharmonic contribution to more than 9% for the model of the heat capacities (Liu et al. 2019b).

Noted that iron is a crucial element in olivine, the most abundant and important mineral in the upper mantle, and the solid solutions of $Mg_{2-x}Fe_xSiO_4$ between forsterite (Fo, Mg_2SiO_4) and fayalite (Fa, Fe_2SiO_4) have been widely studied (e.g., Gaisler and Kolesov 2007; Ishibashi et al. 2012; Breitenfeld et al. 2018). The olivines in the upper mantle are generally believed to have Fe# values ranging from 5 to 15, and the San Carlos olivine samples typically have Fe# values of 9 to 13. To investigate the iron effect on the thermodynamic properties, we collected in situ high-temperature and high-pressure Raman spectra on

* E-mail: yeyu@cug.edu.cn

0003-004X/21/0010–1668$05.00/DOI: https://doi.org/10.2138/am-2021-7686

two olivine samples of natural $Fo_{89}Fa_{11}$ and synthetic $Fo_{58}Fa_{42}$. The results may provide important constraints on compositional (such as Fe) effect on the thermodynamic properties of the main minerals in the upper mantle.

Experimental procedures

Sample synthesis and characterization

Commercial chemical reagents FeO, MgO, SiO_2, and Fe (from Alfa-Aesar company, purities >99.95%, particle sizes <2 μm) were used for synthesis of the Fe-rich olivine sample. First, we synthesized the two end-members of fayalite (Fe_2SiO_4) and forsterite (Mg_2SiO_4) at ambient pressure and high temperature. Two mixtures of FeO+SiO_2 and MgO+SiO_2 were prepared with a molar ratio of 2:1.002 and ground with acetone in a mortar for at least 2 h, individually. A small amount of metallic Fe powders (~5% by weight) were added to the mixture of FeO+SiO_2 to reduce the oxygen fugacity in the synthesis of fayalite. Each mixture was cold compressed into a pellet using a hydraulic press and then encapsulated in an Ar-filled-sealed steel tube. Both tubes were placed in an Al_2O_3 furnace and heated at T = 1423 K for 24 h. Next, each of the samples was removed from the tube, reground in a mortar, compressed to a new pellet, sealed again in a new tube, and put back to the furnace for a second run of sintering at 1423 K for 48 h. The purities of synthesized fayalite and forsterite samples were checked by powder X-ray diffraction.

Next, the powders of fayalite and forsterite were mixed in a molar ratio of ~2:3 and ground with acetone for 5 h. This mixed material was compressed in a graphite chamber, which was then loaded in a 150-ton non-end-loaded piston-cylinder apparatus (Wang et al. 2010). The synthetic experiment was carried out at P = 1.5 GPa and T = 1473 K for 24 h. Pressure calibration was conducted against the albite/jadeite + quartz phase transition with an uncertainty of ±0.1 GPa, and the temperature was monitored by a type C thermocouple (W5Re95-W26Re74) at the center of the furnace with an uncertainty of ±10 °C. The quenched sample chamber was cut open, and the product was characterized by Raman spectroscopy.

The synthetic Fe-rich olivine sample and a natural San Carlos olivine sample (from a peridotite rock collected in Arizona, U.S.A.) were adopted for measurements in this study. Chemical composition analysis was conducted on two selected chips (with diameters of ~200 μm) from these samples. Both sample chips were polished on the top sides in epoxy, and coated with a thin conductive carbon film. Next, measurements were conducted with a JEOL JXA-8230 electron probe microanalyzer (EPMA), which was equipped with five wavelength-dispersive spectrometers (WDS) and operated at an accelerating voltage of 15 kV and a beam current of 20 nA. We used a spot size of 5 μm to minimize X-ray intensity fluctuations (Wang et al. 2019). The certified mineral standards (olivine for Mg and Si, garnet for Fe and Mn, wollastonite for Ca, ilmenite for Ti, corundum for Al, nickel metal for Ni, and chromium metal for Cr) were selected for quantification with ZAF (atomic number, absorption, and fluorescence) wavelength-dispersive corrections. At least 9 points were measured at different locations in each sample, and the averaged oxide weights are listed in Table 1. The formulas are expressed as $Mg_{1.748}Fe_{0.222}Ni_{0.006}Ca_{0.002}Mn_{0.003}Si_{1.006}O_4$ for the natural San Carlos olivine ($Fo_{89}Fa_{11}$ hereafter) and $Mg_{1.151}Fe_{0.837}Ca_{0.006}Mn_{0.001}Si_{1.001}O_4$ for the synthetic sample ($Fo_{58}Fa_{42}$ hereafter), while ferrous iron (Fe^{2+}) was assumed to be dominant in these Fe-bearing olivine samples.

It should be noted that Abdu et al. (2008) synthesized a $Fo_{55}Fa_{45}$ olivine sample from the starting materials Fe_2O_3+MgO+SiO_2 with a graphite buffer, and the Mössbauer spectra of the product show that nearly all the iron cations are ferrous, without any detection of Fe^{3+}. In addition, the water contents in both the natural and synthetic samples are estimated to be <20 ppm by weight, according to the measured IR spectra. Such low H_2O concentrations should not have significant impact on the thermodynamic properties at high temperatures.

High-temperature and high-pressure Raman spectra

In situ Raman spectra under high-temperature and high-pressure conditions were measured on a Horiba LabRAM HR Evolution system with a micro confocal Raman spectrometer. A green beam (λ = 532 nm, the second harmonic of the baseline at 1064 nm) was excited from a Nd YAG laser source operated at 20 mW, and the spectrometer was calibrated with a silicon single crystal. Under ambient condition, we also collected Raman spectra on these two samples with a red beam (λ = 633 nm) for comparison, which was excited from a helium-neon gas laser source at 10 mW, and the Raman spectra collected at the 532 and 633 nm excitations are quite consistent with each other (Online Material[1] Fig. OM1). For both the high-temperature experiment inside the heating stage and high-pressure measurement inside diamond-anvil cells (DACs), the Raman spectra (in the frequency range of 100–1200 cm^{-1}) were collected in the backscattering direction through a VIS LWD 50× objective (the focal distance is 10.60 mm, and the numerical aperture is 0.25).

In the high-temperature measurements, two chips from the natural $Fo_{89}Fa_{11}$ (250 × 200 × 100 $μm^3$) and synthetic $Fo_{58}Fa_{42}$ (150 × 100 × 80 $μm^3$) samples were individually loaded on the sapphire plate inside a Linkam THMS 1500 heating stage. Raman spectra of $Fo_{89}Fa_{11}$ and $Fo_{58}Fa_{42}$ were obtained at high temperatures up to 1243 and 893 K, respectively, with an interval of 50 K and a heating rate of 10 K/min. High temperatures were generated by a resistance heater inside the sample chamber and controlled by an automatic temperature controlling unit with an uncertainty <5 K. The sample chamber was filled with N_2 gas throughout the high-temperature measurements on these Fe-bearing samples. To ensure thermal equilibrium, each target temperature was held for ~5 min before measurement, and Raman spectrum was collected in 12 min with an accumulation of 4 times.

Two diamond anvils with 300 μm culets were aligned in a symmetric-type diamond-anvil cell for high-pressure Raman measurements. A rhenium gasket was pre-indented to a thickness of ~30 μm with a 150 μm diameter hole. Two selected sample chips from $Fo_{89}Fa_{11}$ (40 × 45 × 20 $μm^3$) and $Fo_{58}Fa_{42}$ (20 × 20 × 15 $μm^3$) were loaded with an annealed ruby chip (3 μm in diameter). The ruby fluorescence line $R1$ was measured at 694.5 nm prior to gas loading. Argon was adopted as the pressure-transmitting medium, and cryogenic loading of liquid Ar was fulfilled by cooling with liquid N_2. At each pressure step, a Raman spectrum was obtained on each sample over a duration of 22 min with an accumulation of 4 times. The ruby R1 line was measured immediately before and after the collection of each spectrum, and pressures were calculated on the ruby scale from Ye et al. (2018). The difference between the pressures measured before and after each spectrum was typically within 0.4 GPa.

Table 1. Electron microprobe analyses for the olivine samples

	$Fo_{89}Fa_{11}$	$Fo_{58}Fa_{42}$		$Fo_{89}Fa_{11}$	$Fo_{58}Fa_{42}$
SiO_2 (wt%)	40.89(10)	36.03(14)	Si (apfu[a])	1.006(2)	1.001(4)
MgO	47.51(9)	27.78(17)	Mg	1.748(3)	1.151(7)
Al_2O_3	0.01(1)	0.02(1)	Al	0.000(0)	0.001(0)
MnO	0.14(1)	0.03(1)	Mn	0.003(0)	0.001(0)
Cr_2O_3	0.02(1)	0.01(0)	Cr	0.000(0)	0.000(0)
CaO	0.07(0)	0.22(1)	Ca	0.002(0)	0.006(0)
FeO[b]	10.78(5)	36.03(13)	Fe	0.222(1)	0.837(3)
NiO	0.32(0)	0.00(0)	Ni	0.006(0)	0.000(0)
TiO_2	0.00(0)	0.01(0)	Ti	0.000(0)	0.000(0)
Total	99.74(8)	100.13(17)			

[a] The number of oxygen atoms is fixed at 4.
[b] All Fe in these samples is assumed to be Fe^{2+}.

Results and discussion

Fe effect on Raman spectra

There are 84 vibrational modes in the structure of $(Mg,Fe)_2SiO_4$ olivine (space group: *Pbnm*, Z = 4), including 3 acoustic modes, 36 Raman-active modes, 35 IR-active modes, and 10 inactive modes (e.g., Fateley et al. 1971; Farmer and Lazarev 1974; Iishi 1978; Hofmeister 1987; Rao et al. 1988; Chopelas 1991; Kolesov and Geiger 2004; McKeown et al. 2010). On the other hand, the 81 optical modes can be divided into three groups: (1) 45 lattice vibrations in the frequency range below 500 cm^{-1} (including translations of divalent metallic cations as well as translations and rotations of SiO_4 tetrahedra); (2) 8 symmetric (ν_2) and 12 asymmetric (ν_4) O-Si-O bending modes in the range of 370–700 cm^{-1}; (3) 4 symmetric (ν_1) and 12 asymmetric (ν_3) Si-O stretching modes in the range from 800 to 1200 cm^{-1}.

The Raman spectra for $Fo_{89}Fa_{11}$ and $Fo_{58}Fa_{42}$ under ambient conditions are shown in Figure 1 with the fitted vibrational frequencies listed in Table 2. Four internal Si-O stretching vibrational bands (both ν_1 and ν_3) are observed at 819, 849, 914, and 945 cm^{-1} for $Fo_{58}Fa_{42}$ and at 823, 855, 919, and 960 cm^{-1} for $Fo_{89}Fa_{11}$. Three O-Si-O asymmetric bending modes are detected at 532, 576, and 604 cm^{-1} for $Fo_{58}Fa_{42}$, while at 542, 580, and

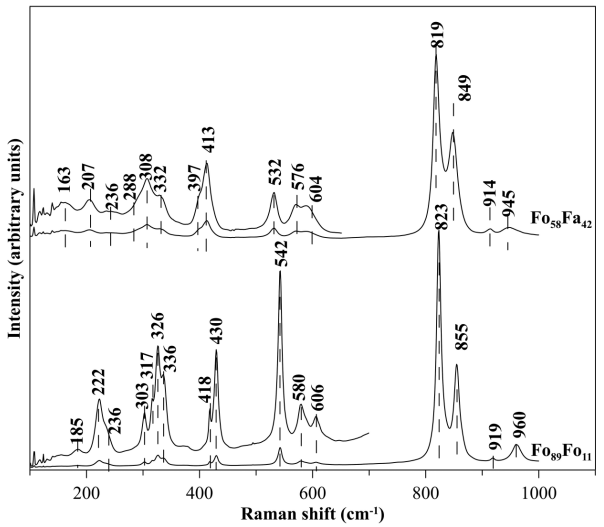

Figure 1. Raman spectra of $Fo_{89}Fa_{11}$ and $Fo_{58}Fa_{42}$ under ambient condition, with the fitted peak positions labeled. The signals below 700 cm^{-1} are magnified for clarity.

606 cm^{-1} for $Fo_{89}Fa_{11}$. The internal modes are generally accepted to shift systematically to lower frequencies with increasing Fe concentration in the $Fe_xMg_{2-x}SiO_4$ solid solutions of olivine (Burns and Huggins 1972; Guyot et al. 1986; Kolesov and Tanskaya 1996; Gaisler and Kolesov 2007; Mouri and Enami 2008; Ishibashi et al. 2012; Breitenfeld et al. 2018). For example, the Raman shifts of the two strongest modes in the ranges of 812–828 and 835–860 cm^{-1} have been proposed as a quick tool to estimate Fe contents in $Fe_xMg_{2-x}SiO_4$ solid solutions (Ishibashi et al. 2012; Breitenfeld et al. 2018). The measured vibrational frequencies for these two olivine samples correspond to compositions of $Fo_{85}Fa_{15}$–$Fo_{91}Fa_9$ and $Fo_{55}Fa_{45}$–$Fo_{58}Fa_{42}$, respectively, which are consistent with the accurate results from EPMA.

In addition, Chopelas (1991) also noted the phenomenon that the SiO_4 internal modes show negative dependences on the atomic weight of the divalent metallic cations among the phases, including forsterite (Mg_2SiO_4), monticellite ($CaMgSiO_4$), γ-Ca_2SiO_4, tephroite (Mn_2SiO_4), and fayalite (Fe_2SiO_4). Substitution by heavier metallic cations (such as Fe^{2+}) in the olivine structure may weaken the internal vibrations inside the isolated SiO_4 tetrahedra.

Raman spectra at high temperature

Selected high-temperature Raman spectra on $Fo_{89}Fa_{11}$ and $Fo_{58}Fa_{42}$ are shown in Figures 2a–2b. As temperature increases, the Raman signals get weaker and broader, while the black-body radiation becomes stronger. At temperatures above 1200 K, identifying and fitting the weak bands is very difficult in the frequency range below 500 cm^{-1} for $Fo_{89}Fa_{11}$, while these lattice vibrations at low frequencies play an important role in determining the anharmonic contribution to thermodynamic properties. Hence, we only recorded the Raman spectra up to 1193 K for this sample. Eight to nine lattice vibrations (below 500 cm^{-1}) can still be distinguished in the spectra (although very weak) when collected through the sapphire window in the heating stage at

Table 2. Frequencies of Raman modes, corresponding temperature/pressure derivatives, isobaric mode Grüneisen parameters, isothermal mode Grüneisen parameters, and intrinsic anharmonic parameters of $Fo_{89}Fa_{11}$, $Fo_{58}Fa_{42}$ olivine samples

Symmetry	v_i at ambient condition (cm^{-1})	$(\partial v_i/\partial T)_P$ (cm^{-1} K^{-1})	γ_{iP}	$(\partial v_i/\partial P)_T$ (cm^{-1} GPa^{-1})	γ_{iT}	a_i (10^{-5} K^{-1})	Mode assignment
			$Fo_{89}Fa_{11}$				
A_g	960	−0.026(1)	0.75(1)	4.22(8)	0.57(1)	−0.65(4)	v_3
B_{3g}	919	−0.025(8)	0.77(5)	2.76(8)	0.39(1)	−1.39(1)	v_3
B_{2g}	882			2.67(5)	0.39(4)		v_3
A_g	855	−0.016(3)	0.52(7)	2.74(4)	0.41(7)	−0.39(8)	v_1+ v_3
A_g	823	−0.018(9)	0.63(4)	3.00(5)	0.47(4)	−0.58(1)	v_1+ v_3
A_g	606	−0.016(8)	0.76(6)	2.96(8)	0.63(6)	−0.46(7)	v_4
B_{1g}	580	−0.009(7)	0.46(2)	1.89(9)	0.42(2)	−0.14(5)	v_4
A_g	542	−0.010(2)	0.51(9)	1.90(2)	0.45(5)	−0.23(2)	v_4
B_{3g}	430	−0.022(1)	1.42(1)	5.20(q)	1.54(9)	0.46(4)	v_2
A_g	418	−0.027(1)	1.78(3)	4.84(1)	1.51(1)	−0.98(5)	v_2
A_g	336	−0.040(1)	3.29(9)	4.61(5)	1.78(6)	−5.47(9)	R(SiO_4)+T($M2O_6$)
A_g	326	−0.017(8)	1.50(6)				R(SiO_4)+T($M2O_6$)
B_{1g}	317	−0.026(4)	2.30(4)	3.29(1)	1.35(0)	−3.45(2)	R(SiO_4)+T($M2O_6$)
A_g	303	−0.021(8)	1.99(1)	2.71(4)	1.16(3)	−2.99(3)	R(SiO_4)+T($M2O_6$)
B_{2g}	236	−0.008(3)	1.12(1)				T(SiO_4)+T($M2O_6$)
A_g	222	−0.009(6)	1.03(1)	0.88(8)	0.51(9)	−1.85(6)	T(SiO_4)+T($M2O_6$)
A_g	185	−0.019(9)	2.96(7)				T(SiO_4)+T($M2O_6$)
			$Fo_{58}Fa_{42}$				
A_g	945	−0.021(2)	0.65(7)	4.42(6)	0.59(1)	−0.22(5)	v_3
B_{3g}	914	−0.024(5)	0.78(5)	3.01(8)	0.41(8)	−1.25(3)	v_3
A_g	849	−0.010(6)	0.36(6)	2.97(3)	0.44(4)	0.26(9)	v_1+v_3
A_g	819	−0.019(1)	0.68(3)	2.90(3)	0.44(9)	−0.79(9)	v_1+v_3
A_g	604	−0.024(5)	1.18(9)	3.10(3)	0.65(1)	−1.83(4)	v_4
B_{3g}	576	−0.015(5)	0.78(7)	4.15(2)	0.92(4)	0.46(7)	v_4
A_g	532	−0.009(6)	0.52(9)	1.73(4)	0.41(4)	−0.39(4)	v_4
B_{3g}	413	−0.019(4)	1.35(9)	3.81(3)	1.17(1)	−0.64(4)	v_2
A_g	397			4.70(3)	1.49(8)		v_2
B_{1g}	357	−0.031(4)	2.58(3)				T($M2O_6$)
B_{1g}	332	−0.033(6)	3.00(8)	3.48(7)	1.34(3)	−5.53(5)	T($M2O_6$)
A_g	308	−0.041(5)	3.94(8)	4.34(8)	1.79(2)	−7.36(3)	R(SiO_4)+T($M2O_6$)
A_g	288	−0.031(3)	3.18(5)	4.21(1)	1.85(8)	−4.53(5)	R(SiO_4)+T($M2O_6$)
B_{1g}	236	−0.013(1)	1.62(1)	2.26(4)	1.21(4)	−1.38(9)	T(SiO_4)+T($M2O_6$)
A_g	207	−0.006(1)	0.86(3)	1.30(4)	0.79(8)	−0.22(2)	T(SiO_4)+T($M2O_6$)
A_g	163	−0.013(6)	2.43(9)				T(SiO_4)+T($M2O_6$)

Notes: T = translation. R = rotation.

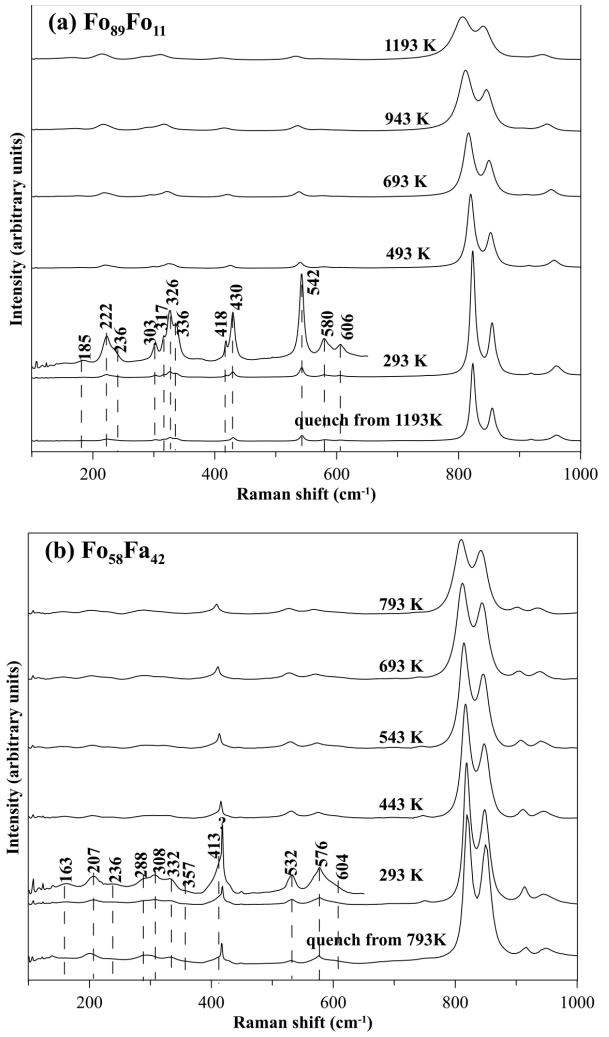

Figure 2. Selected high-temperature Raman spectra for (**a**) $Fo_{89}Fa_{11}$ and (**b**) $Fo_{58}Fa_{42}$, with the background subtracted. The spectrum collected when quenched to room temperature is also presented for each sample. The weak bands in the frequency range below 700 cm^{-1} are labeled and magnified for clarity at T = 300 K.

high temperatures. Another spectrum was collected after the sample was quenched from 1193 K. This spectrum is consistent with that for olivine, showing no phase transformation throughout the heating procedure. According to the phase diagram of $Mg_{1.84}Fe_{0.16}SiO_4$–O_2 (Michel et al. 2013), the $Fo_{92}Fa_8$ sample would dissociate to an assemblage of Fe_2O_3+Mg_2SiO_4+$MgSiO_3$ (orthoenstatite) at T = 773 K in an oxygen pressure $P(O_2)$ range of 10^{-3}–10^3 atm. Our Raman measurements on the $Fo_{89}Fa_{11}$ sample showed that it persisted up to a significantly higher temperature under the protection of N_2.

On the other hand, the $Fo_{58}Fa_{42}$ sample is observed to be stable only up to 793 K (refer to the quenched spectra from 793 K in Fig. 2b), while clear phase dissociation occurs at a higher temperature. The Raman spectrum measured after quenching from 893 K (Fig. 3) shows a phase assemblage of γ-Fe_2O_3 maghemite (Chamritski and Burns 2005), ortho-enstatite (Lin 2003), quartz (Fridrichová et al. 2016), and some remaining olivine with weakened signals as compared with those before heating. As compared with $Fo_{89}Fa_{11}$, the $Fo_{58}Fa_{42}$ sample dissociates at a relatively lower temperature due to Fe incorporation. Abdu et al. (2008) carried out in situ high-temperature Mössbauer measurements on synthetic $Fo_{55}Fa_{45}$ olivine with pressure evacuated to ~10^{-8} atm in the chamber and detected the appearance of metallic iron at temperatures above 923 K. Hence, it is possible that at temperatures above 900 K, part of ferrous iron (Fe^{2+}) in these Fe-rich olivine samples might dissociate to ferric iron (Fe^{3+}) as in Fe_2O_3 and metallic Fe ($3Fe^{2+} = 2Fe^{3+} + Fe^0$) even at very low O_2 pressures (low O_2 fugacities).

Variations of the fitted vibrational frequencies are plotted as a function of temperature in Figures 4a–4c. All the Raman bands systematically shift to lower frequencies with increasing temperature, and linear regression is fitted for each mode with the slope, $(\partial\nu_i/\partial T)_P$ (cm^{-1}/K) listed in Table 2. Some of the lattice vibrations (including four modes in the range of 280 ~ 360 cm^{-1} for $Fo_{58}Fa_{42}$ and one mode at 336 cm^{-1} for $Fo_{89}Fa_{11}$) show negative temperature dependences with magnitudes >0.03 cm^{-1}/K, which are also larger than those for Mg-end-member forsterite samples (Gillet et al. 1991, 1997; Yang et al. 2015). In addition, the modes (A_g and B_{1g}) above 900 cm^{-1} are observed to decrease at larger rates (>0.02 cm^{-1}/K) with increasing temperature than those (0.01–0.02 cm^{-1}/K) for other internal modes at lower frequencies, which has also been reported for the Fo_{100} samples.

Pressure effect on the vibrational modes and their splitting

High-pressure Raman spectra were measured on both $Fo_{89}Fa_{11}$ and $Fo_{58}Fa_{42}$ up to 19 GPa without any phase transition at T = 300 K, while a phase transition in forsterite has been observed at a higher pressure of ~50 GPa and room temperature (Finkelstein et al. 2014). According to Klotz et al. (2009), the pressure gradients inside the solid Ar medium are <0.2 GPa in the pressure range below 20 GPa, which is smaller than the estimated uncertainties for the measurements. Selected Raman spectra at various pressures are shown in Figures 5a–5b for the two olivine

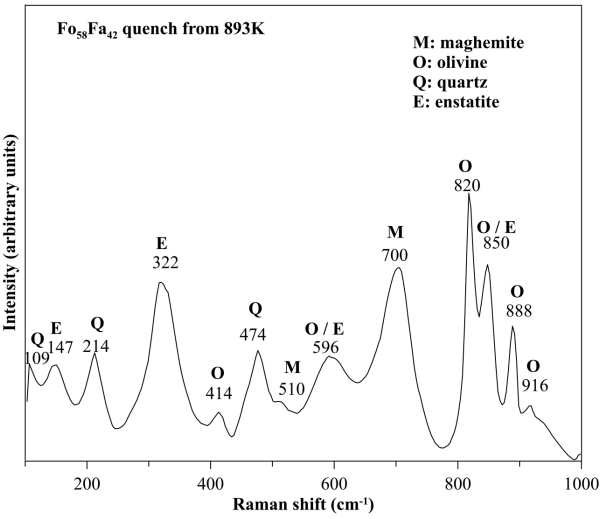

Figure 3. Raman spectra collected when quenched to room temperature after dissociation of $Fo_{58}Fa_{42}$ at 893 K.

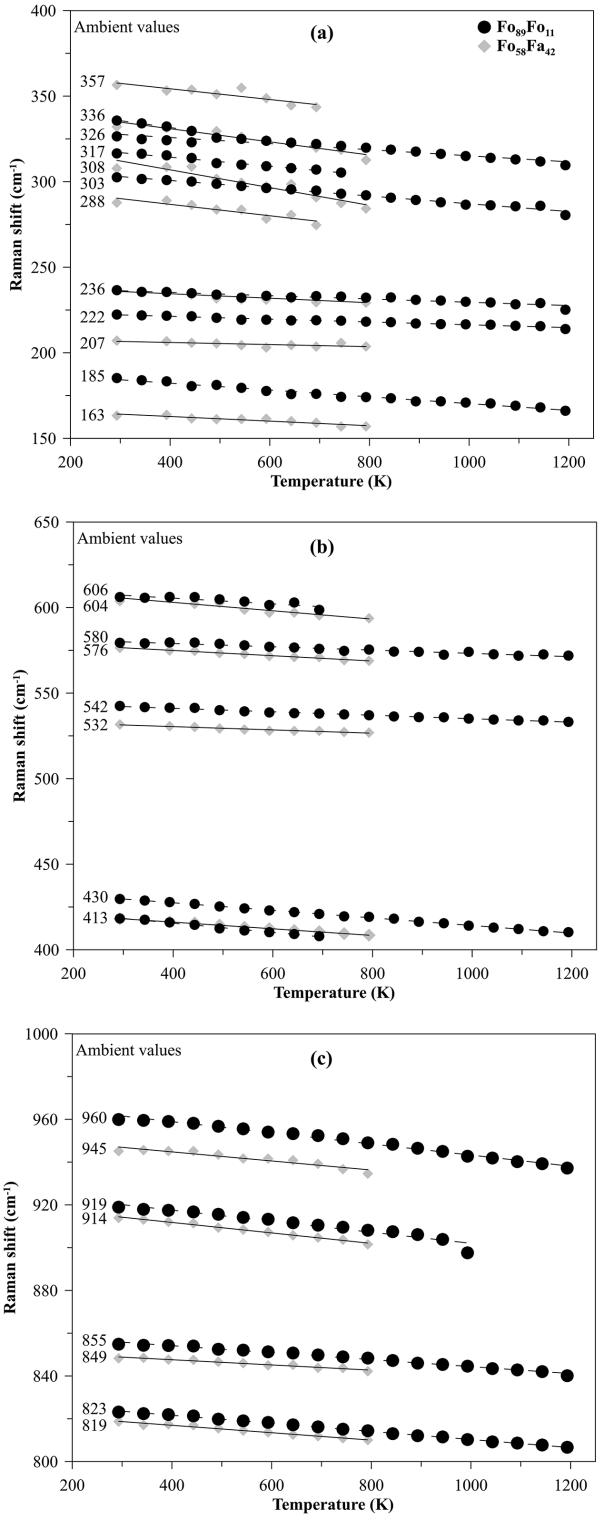

Figure 4. Temperature dependence of the vibrational modes for both the $Fo_{89}Fa_{11}$ (black) and $Fo_{58}Fa_{42}$ (gray) samples with a linear regression line for each vibration, in the ranges of (**a**) 100–400 cm^{-1}, (**b**) 400–800 cm^{-1}, and (**c**) 800–1000 cm^{-1}. The peak positions at 293 K are labeled at the left sides of the figures. Linear regression is fitted for each data set.

samples. 10 to 13 bands for the lattice vibrations are detected in spectra collected through the diamond window inside the DAC up to 19 GPa. All the Raman-active modes systematically shift to higher frequencies at elevated pressures (Figs. 6a–6c), due to the contraction of the olivine structure. Linear regressions are fitted between the vibrational frequencies and pressure, and the slopes of $(\partial v_i/\partial P)_T$ (cm^{-1}/GPa) are listed in Table 2. The frequencies typically increase at rates of 2–4 cm^{-1}/GPa at elevated pressures for both the olivine samples. In addition, the signals collected through the diamond windows in the high-pressure measurements become relatively weaker, especially for the weak lattice vibrations in the low-frequency range. A few lattice vibrational modes below 400 cm^{-1} (such as the ones at 185, 236, and 326 cm^{-1} for the $Fo_{89}Fa_{11}$ sample), which had been observed in the high-temperature experiment (describe above), could not be identified in the Raman spectra collected from DAC.

On the other hand, the isolated SiO_4 tetrahedra are distorted

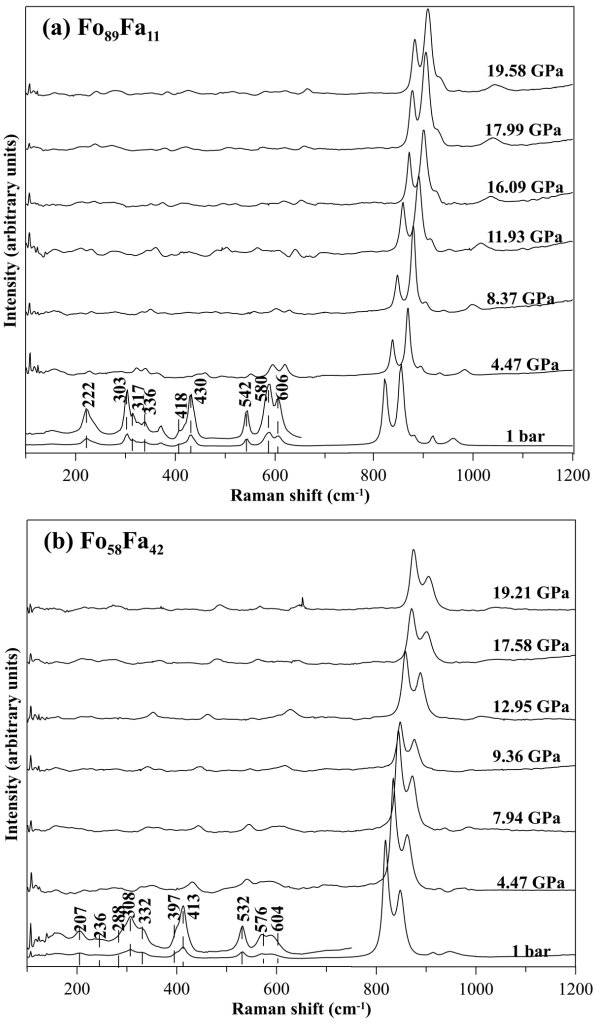

Figure 5. Representative Raman spectra of (**a**) $Fo_{89}Fa_{11}$ and (**b**) $Fo_{58}Fa_{42}$ measured at high pressures, with the background subtracted. The modes with small intensities below 700 cm^{-1} are labeled and magnified for clarity.

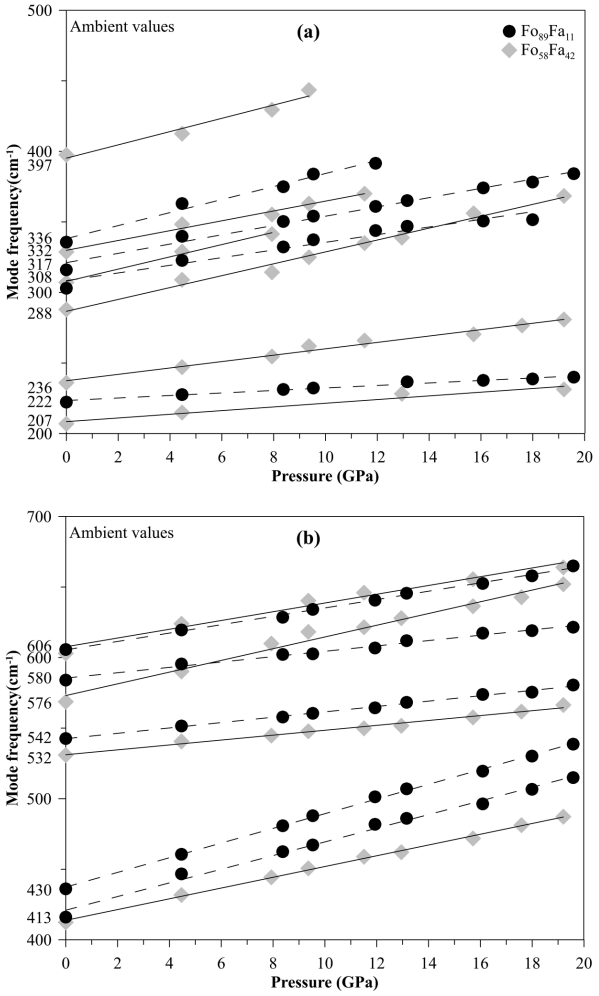

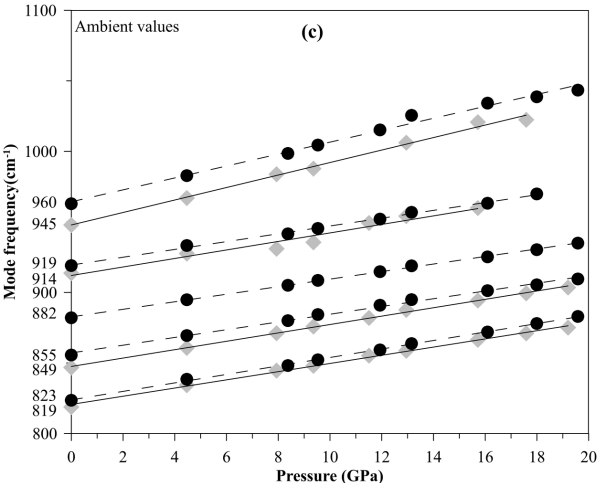

◄▲**FIGURE 6.** Pressure dependence of the Raman-active modes for $Fo_{89}Fa_{11}$ (black) and $Fo_{58}Fa_{42}$ (gray) in the frequency ranges of (**a**) 100–400 cm^{-1}, (**b**) 400–800 cm^{-1}, and (**c**) 800–1000 cm^{-1}, with linear regression for each vibrational data set.

in the olivine structure due to the static crystal-field forces, as well as dynamical interactions between SiO_4 units. Consequently, the number of internal modes is increased to 24 from 9 (for an undistorted SiO_4 tetrahedron with T_d symmetry, $3\nu_4 + 2\nu_2 + 1\nu_1 + 3\nu_3$). In addition to these mode-splitting factors, coupling between modes at different energy states also contributes to the complicated lattice-dynamic behavior in olivine (Hohler and Funck 1973; Piriou and McMillan 1983). Kolesov and Geiger (2004) noted that the static crystal-field splitting gets weakened at elevated temperatures. They measured the two A_g modes at ~960 and 820 cm^{-1} (the highest and lowest symmetric energy states of a split ν_3 vibration) for Fo_{100} and $Fo_{90}Fa_{10}$, and found that the frequency difference $A_g(960)$–$A_g(820)$ decreases with increasing temperature, which is consistent with the high-temperature data presented in Gillet et al. (1991) and this study (Fig. 7a). The value of $A_g(960)$–$A_g(820)$ decreases at rates of –0.008 cm^{-1}/K for $Fo_{89}Fa_{11}$ and –0.002 cm^{-1}/K for $Fo_{58}Fa_{42}$.

Our high-pressure Raman measurement shows that the difference of $A_g(960)$–$A_g(820)$ increases at a rate of +1.2 cm^{-1}/GPa for $Fo_{89}Fa_{11}$ and +1.5 cm^{-1}/GPa for $Fo_{58}Fa_{42}$ (Fig. 7b), indicating that the crystal-field splitting force is strengthened at elevated pressures, as opposed to the temperature effect. Furthermore, the $A_g(960)$ mode exhibits a larger pressure dependence than $A_g(820)$ in forsterite (Fo_{100}) samples (Chopelas 1990; Gillet et al. 1991; Wang et al. 1993; Liu and Mernagh 1993; Hushur et al. 2009) and $Fo_{97}Fa_3$ (Manghnani et al. 2013), which would yield larger values of $A_g(960)$–$A_g(820)$ at elevated pressures as well (Fig. 7b). According to the scheme of the static and dynamic splitting of the internal stretching modes in the olivine structure (Kolesov and Geiger 2004), the B_{3g} mode at 920 cm^{-1} and the B_{2g} mode at 880 cm^{-1} are caused by the dynamic splitting effect. The difference in B_{3g}–B_{2g} remains almost constant at high pressures for this $Fo_{89}Fa_{11}$ sample and Fo_{100} (Chopelas 1990) (Fig. 7c), suggesting that the dynamic splitting is nearly independent of pressure and largely controlled by the O-O interactions between SiO_4 units.

Grüneisen parameters and intrinsic anharmonicity

The temperature and pressure dependences of the vibrational frequency (ν_i, cm^{-1}) are determined by two parts: pure volumetric variation under high-pressure and high-temperature conditions and pure temperature and pressure contributions arising from intrinsic anharmonicity (e.g., Gillet et al. 1991). The isobaric (γ_{iP}) and isothermal (γ_{iT}) mode Grüneisen parameters, which describe the variation of ν_i with temperature and pressure are calculated in Equations 1–2, respectively. Next, the intrinsic anharmonic parameters (a_i, K^{-1}), describing the variation of ν_i with temperature at a constant volume, are related to the difference between γ_{iP} and γ_{iT} (Eq. 3):

$$\Upsilon_{iP} = \left(\frac{\partial \ln \nu_i}{\partial \rho}\right)_P = -\frac{1}{\alpha \nu_{0i}}\left(\frac{\partial \nu_i}{\partial T}\right)_P \quad (1)$$

$$\Upsilon_{iT} = \left(\frac{\partial \ln \nu_i}{\partial \rho}\right)_T = \frac{K_T}{\nu_{0i}}\left(\frac{\partial \nu_i}{\partial P}\right)_T \quad (2)$$

$$\alpha_i = \left(\frac{\partial \ln \nu_i}{\partial T}\right)_V = -\alpha\left(\Upsilon_{iP} - \Upsilon_{iT}\right). \quad (3)$$

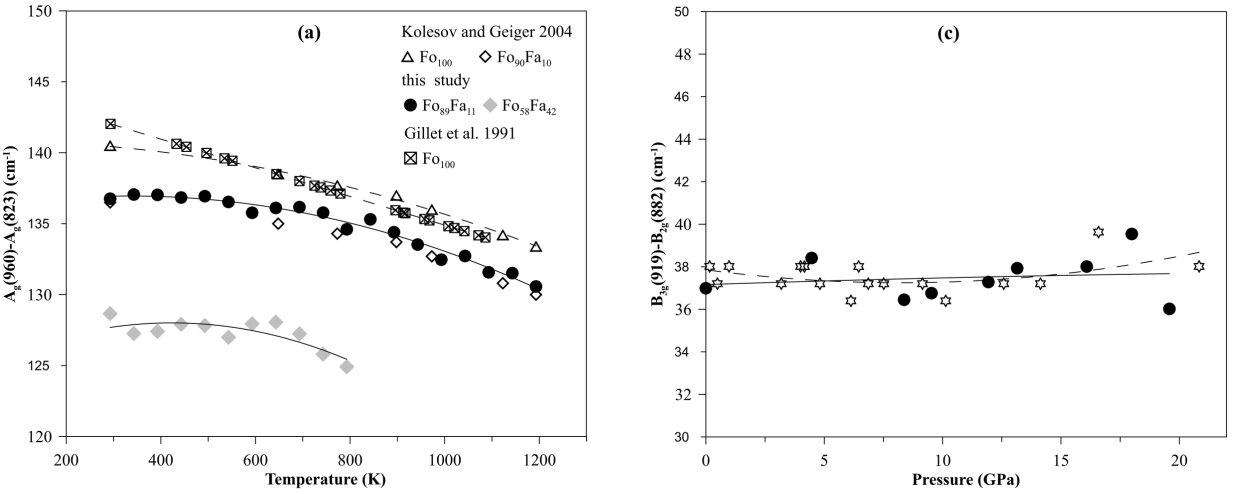

◀▲**FIGURE 7.** Frequency difference between the coupled ν_3–ν_1 stretching modes as a function of (**a**) temperature and (**b**) pressure, and the difference between the dynamically splitted B_{3g} and B_{2g} modes as a function of (**c**) pressure for the olivine samples (Chopelas 1990; Gillet et al. 1991; Kolesov and Geiger 2004; Hushur et al. 2009; this study).

where υ_{0i} is the mode frequency under ambient conditions, while α and K_T are the thermal expansion coefficient and isothermal bulk modulus, respectively. Adopting the averaged volume thermal expansion coefficients of 3.62×10^{-5} K^{-1} for $Fo_{89}Fa_{11}$ and 3.41×10^{-5} K^{-1} for $Fo_{58}Fa_{42}$ (Kroll et al. 2012), as well as the isothermal bulk moduli of 129.9 GPa for $Fo_{89}Fa_{11}$ (Zha et al. 1998) and 126.6 GPa for $Fo_{58}Fa_{42}$ (Nestola et al. 2011), we calculated the γ_{iP} and γ_{iT} mode Grüneisen parameters and harmonic a_i parameters for both the olivine samples (Table 2).

The obtained isobaric and isothermal mode Grüneisen parameters for $Fo_{89}Fa_{11}$ and $Fo_{58}Fa_{42}$ are compared with those of Fo_{90} (Kolesov and Geiger 2004) and Fo_{100} (Chopelas 1990; Gillet et al. 1991; Kolesov and Geiger 2004; Hushur et al. 2009) in Figures 8a and 8b, respectively. The mode Grüneisen parameters typically range from 0.3 to 1.2 for the internal modes (ν_4, ν_1, and ν_3) in the frequency range above 500 cm^{-1}, which are systematically smaller than the macroscopic Grüneisen parameters extracted from heat capacity and thermal expansivity ($\gamma = 1.24$ for Fo_{100} and 1.30 for Fa_{100} at $T = 300$ K) (Kroll et al. 2012). For lattice vibrations in the lower frequency range, the γ_{iP} and γ_{iT} parameters are distributed in the ranges of 0.6~3.9 and 0.5~2.1, respectively. The translations of the isolated SiO_4 units and metallic cations are more sensitive to variations of temperature and pressure, as compared with the O-Si-O bending and Si-O stretching vibrations inside SiO_4 tetrahedra, as rigid bodies.

The intrinsic anharmonic parameters for the Fe-bearing and Mg-end-member samples are shown in Figure 8c. All the a_i parameters for both lattice and internal vibrations are negative, implying that the harmonic approximation underestimates the thermodynamic properties (such as heat capacities, internal energy, and entropy). The internal modes exhibit anharmonic parameters typically ranging from 0 to –2, while some of the lattice vibrations show a_i values with much larger magnitudes. Hence, the lattice vibrations should play a more important role than the internal modes in the anharmonic contributions to thermodynamic properties of olivine. There are 84 vibrations in the olivine structure from theoretical prediction, while fewer modes can be measured in Raman spectra (e.g., Gillet et al. 1991). To estimate the anharmonic contributions to the thermodynamic properties, we calculated the averaged a_i parameters for each vibrational continuum (Table 3) on the basis of the anharmonic mode parameters listed in Table 2. For Fo_{100}, the lowest frequency at 105 cm^{-1} is taken from the inelastic neutron measurement (Rao et al. 1988), and the other cutoff frequencies for the optic continua are from the models by Kieffer (1979) and Hofmeister (1987). For the Fe-bearing samples, we estimated the upper and lower limits of each continuum according to the Fe-concentration dependence of the vibrational frequencies (Hofmeister 1987, 1997; Chopelas 1991).

The anharmonic contribution to thermodynamics

In the Debye model for the harmonic approximation of lattice vibrations, the contribution to the internal energy (U) is composed of a set of continua (e.g., Kieffer 1979; Gillet et al. 1991):

$$U(T) - U(0\text{K}) = 3 \cdot n \cdot \text{R} \sum_{i=1}^{m} \frac{ni}{N} \int_{x_{li}}^{x_{ui}} \frac{x_i T\left[1+\exp(x_i)\right] dx_i}{2(x_{ui}-x_{li})\left[\exp(x_i)-1\right]} = 3 \cdot \frac{n}{N} \cdot \text{R} \sum_{i=1}^{N} U_i^h \quad (4)$$

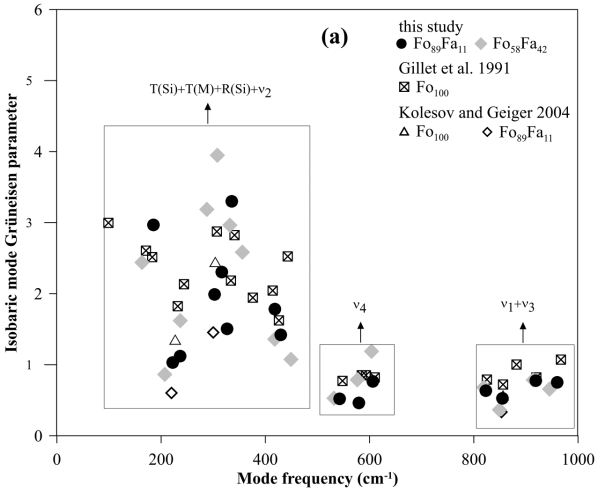

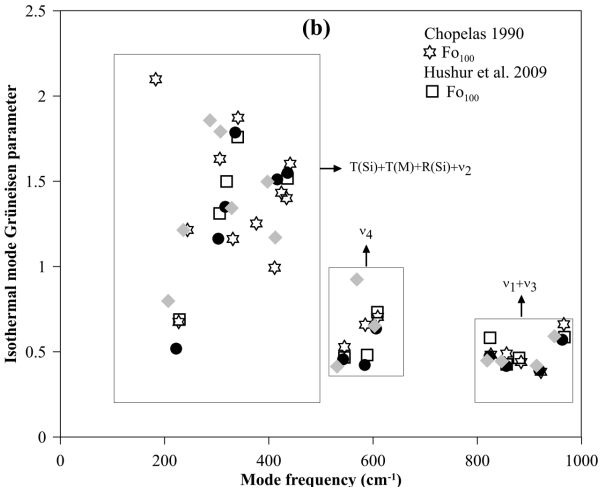

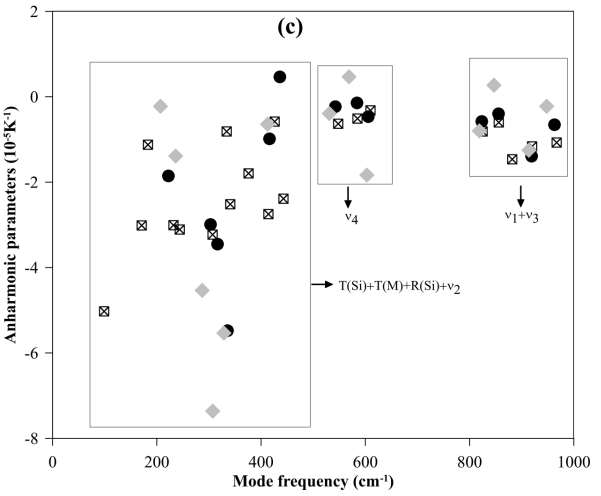

◄▲ **FIGURE 8.** The (**a**) isobaric and (**b**) isothermal mode Grüneisen parameters as well as the intrinsic anharmonic parameters (**c**) for the olivine samples of Fo_{100} (Chopelas 1990; Gillet et al. 1991; Kolesov and Geiger 2004; Hushur et al. 2009), $Fo_{89}Fa_{11}$ (Kolesov and Geiger 2004; this study) and $Fo_{58}Fa_{42}$ (this study).

where U_i^h is the internal energy from the *i*th vibrational mode, and R is the gas constant. The lowercase n ($n = 7$) and uppercase N ($N = 84$) represent the numbers of atoms per formula and total vibrational modes, respectively. The dimensionless frequency $x_i = h \cdot c \cdot \nu_i / (k_B \cdot T)$, where h, c, and k_B are the Planck, light speed, and Boltzmann constants, respectively. The upper (x_{ui}) and lower (x_{li}) frequency limits and the number of vibrational modes (n_i) in each continuum are listed in Table 3. The isochoric (C_V) and isobaric (C_P) heat capacities can be calculated from Equations 5 and 6, respectively:

$$C_V = \left(\frac{\partial U}{\partial T}\right)_V = 3 \cdot n \cdot R \sum_{i=1}^{m} \frac{n_i}{N} \int_{x_{li}}^{x_{ui}} \frac{x_i^2 \exp(x_i)\, dx_i}{(x_{ui} - x_{li})\left[\exp(x_i) - 1\right]^2} = 3 \cdot \frac{n}{N} \cdot R \sum_{i=1}^{N} C_{vi}^h \quad (5)$$

$$C_P = C_v + TV\alpha^2 K_T \quad (6)$$

where C_{vi}^h is the microscopic heat capacity from the *i*th mode. Here, we adopt the thermal expansion coefficients from Kroll et al. (2012) as a function of temperature, as well as the temperature derivative of K_T (–0.023 GPa/K) from Isaak et al. (1989) for calculation. Next, the entropy (S) can be derived as:

$$S(T) - S(0\text{K}) = \int_0^T \frac{C_P}{T} dT. \quad (7)$$

On the other hand, the intrinsic anharmonic parameters (a_i) are needed to compute the anharmonic contributions to the internal energy U and heat capacity C_V:

$$U(T) - U(0\text{K}) = 3 \cdot \frac{n}{N} \cdot R \sum_{i=1}^{m} U_i^h (1 - 2a_i T). \quad (8)$$

$$C_V = 3 \cdot \frac{n}{N} \cdot R \sum_{i=1}^{m} C_{vi}^h (1 - 2a_i T). \quad (9)$$

Based on Equations 4–9, we calculated the thermodynamic properties (internal energy, heat capacities, and entropy) as a function of temperature for $Fo_{89}Fa_{11}$, $Fo_{58}Fa_{42}$, and Fo_{100} (Figs. 9a–9d). In the case of harmonic approximation, the calculated thermodynamic properties (including internal energy, heat capacities, and entropy) are in very good agreement among the three olivine samples (Curves 2, 4, and 6), with a difference typically within

TABLE 3. The averaged intrinsic anharmonic parameters for the optical modes in different optical continua

	No. of modes	Fo_{100}[a]		$Fo_{89}Fa_{11}$[b]		$Fo_{58}Fa_{42}$[b]	
		Frequency range (cm^{-1})	a_i (10^{-5} K^{-1})	Frequency range (cm^{-1})	a_i (10^{-5} K^{-1})	Frequency range (cm^{-1})	a_i (10^{-5} K^{-1})
T(M)+T(M)+R(Si)+ ν_2	52	105–482	–2.0	103–478	–2.4	97–467	–3.3
ν_4	13	505–644	–0.5	499–639	–0.3	478–622	–0.6
$\nu_1+\nu_3$	16	825–975	–1.0	822–973	–0.8	820–963	–0.5

[a] Gillet et al. (1991).
[b] This study.

0.3% even when extrapolated to 2000 K. Hence, the frequency shift caused by Fe incorporation ($\Delta\nu_i$ generally <20 cm^{-1} between Fo_{100} and $Fo_{58}Fa_{42}$) has marginal impact on the thermodynamic properties in the case of harmonic approximation.

Nevertheless, the anharmonic contribution significantly increases the internal energy by large magnitudes of 7, 9, and 12% (at T = 2000 K) for Fo_{100}, $Fo_{89}Fa_{11}$, and $Fo_{58}Fa_{42}$, respectively, with respect to the harmonic approximation. The heat capacities (for both C_V and C_P) increase by 5~6% for Fo_{100}, 6~7% for $Fo_{89}Fa_{11}$, and 9~10% for $Fo_{58}Fa_{42}$, with the contributions of anharmonicity. The anharmonic correction in the entropy is relatively smaller than those in other properties, with the increasing magnitudes of 2 to 3% when extrapolated to 2000 K. Hence, the anharmonic contributions should be taken into account for computing the thermodynamic properties of olivine, especially at high temperatures, while Fe incorporation further increases the magnitudes of these contributions. In addition, the experimental isobaric heat capacities for Fo_{100} (Gillet et al. 1991) and Fa_{100} (Benisek et al. 2012) are consistent with our calculations in the general order of Fo_{100} (experiment, Curve 1) < $Fo_{89}Fa_{11}$ (Curve 3) < $Fo_{58}Fa_{42}$ (Curve 5) < Fa_{100} (experiment) (Fig. 9c); previous calorimetric measurement on Fo_{100} (Gillet et al. 1991) reported C_P heat capacity values about 2 to 4% lower than those calculated (Curve 1) above 1000 K. Moreover, a low-temperature adiabatic calorimetric experiment on the forsterite-fayalite solid solution (Dachs and Geiger 2007) revealed that the C_P values increase with increasing Fe concentration in the temperature range of 70–300 K.

Implications

The intrinsic anharmonic contribution becomes necessary in modeling the thermodynamic properties of olivine, especially at high temperatures (e.g., Gillet et al. 1991; Liu et al. 2019b), and this study reveals that Fe incorporation further increases the magnitudes of these contributions. In addition, previous high-temperature studies have indicated that Fe decreases the thermal expansion coefficients of olivine solid solutions (Smyth and Hazen 1973; Smyth 1975; Hazen 1977; Suzuki et al. 1981; Motoyama and Matsumoto 1989; Redfern et al. 2000; Kroll et al. 2012). This phenomenon may also be related to the

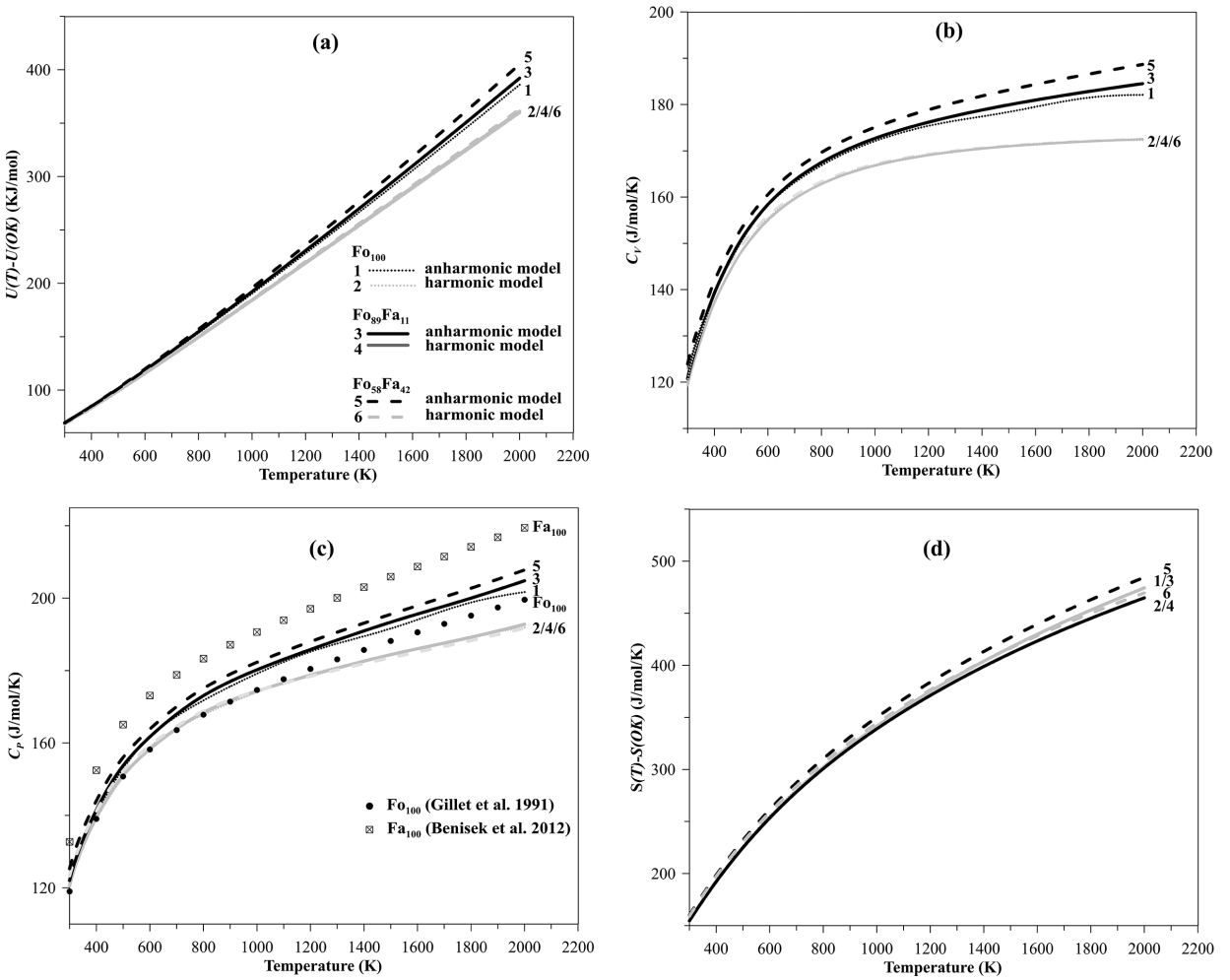

Figure 9. The temperature profiles of the calculated (**a**) internal energy, (**b**) isochoric, and (**c**) isobaric heat capacities, and (**d**) entropy for Fo_{100} (Gillet et al. 1991), $Fo_{89}Fa_{11}$ and $Fo_{58}Fa_{42}$ (this study). The experimental C_P profiles for Fo_{100} (Gillet et al. 1991) and Fa_{100} (Benisek et al. 2012) are also presented in **c**.

Fe effect on anharmonicity, and the theoretical studies have pointed out that intrinsic anharmonicity plays an important role in equations of state for solid minerals at the high-pressure high-temperature (high *P-T*) conditions of the deep Earth interior (e.g., Dorogokupets and Oganov 2004; Oganov and Dorogokupets 2004). Synchrotron X-ray diffraction (XRD) measurements on olivine samples with various Fe concentrations are needed, especially at simultaneously high-pressure and high-temperature conditions, to obtain accurate constraints on the Fe effect on the pressure-volume-temperature (*P-V-T*) equations of state for olivine. Besides, Raman spectra collected at simultaneously high *P-T* conditions can also provide a more precise constraint on the anharmonic contribution to the thermodynamic properties at high pressures.

On the other hand, the equilibrium isotopic fractionations (β-factors) for the elements of O, Si, and Mg in forsterite (Mg-end-member olivine) have been calculated at high *P-T* conditions, on the basis of the calculated vibrational spectra with the harmonic approximation (Wu et al. 2015). Other theoretical studies (e.g., Polyakov and Kharlashina 1994; Polyakov 1998) have demonstrated that the intrinsic anharmonicity also has a significant impact on the pressure dependences of the isotopic fractionation β-factors at high temperatures (refer to Eqs. 21–22 in Polyakov 1998). Thus, the constrained a_i parameters for olivine samples with various Fe concentrations should be useful for evaluating the iron effect on the equilibrium isotopic fractionations of O and Si in olivine at high *P-T* conditions. In conclusion, iron is an important element in many silicate minerals, and its role in the thermodynamics of these minerals (such as olivine) has significant impacts on many physical and chemical properties in the deep interior of the Earth, as well as other planets.

Acknowledgments and Funding

This study was supported by the National Key Research and Development Program of China (Grant No. 2018YFA0702700), the National Natural Science Foundation of China (Grant Nos. 41590621 and 41672041), as well as the Fundamental Research Funds for National Universities, China University of Geosciences (Wuhan). Many thanks are due to Yao Wu for providing the natural San Carlos olivine sample, and Fabin Pan for experimental assistance with EPMA. All experiments were carried out at the State Key Laboratory of Geological Processes and Mineral Resources, China University of Geosciences (Wuhan).

References cited

Abdu, Y.A., Annersten, H., Ericsson, T., and Hawthorne, F.C. (2008) High-temperature cation ordering in olivine: An in situ Mössbauer study of synthetic $(Mg_{0.55}Fe_{0.45})_2SiO_4$. Hyperfine Interactions, 186, 99–103.

Benisek, A., Kroll, H., and Dachs, E. (2012) The heat capacity of fayalite at high temperatures. American Mineralogist, 97, 657–660.

Breitenfeld, L.B., Dyar, M.D., Carey, C.J., Tague, T.J. Jr., Wang, P., Mullen, T., and Parente, M. (2018) Predicting olivine composition using Raman spectroscopy through band shift and multivariate analyses. American Mineralogist, 103, 1827–1836.

Burns, R.G., and Huggins, F.E. (1972) Cation determinative curves for Mg-Fe-Mn olivines from vibrational spectra. American Mineralogist, 57, 967–985.

Chamritski, I., and Burns, G. (2005) Infrared- and Raman-active phonons of magnetite, maghemite, and hematite: A computer simulation and spectroscopic study. Journal of Physical Chemistry B, 109, 4965–4968.

Chopelas, A. (1990) Thermal properties of forsterite at mantle pressures derived from vibrational spectroscopy. Physics and Chemistry of Minerals, 17, 149–156.

——— (1991) Single crystal Raman spectra of forsterite, fayalite, and monticellite. American Mineralogist, 76, 1101–1109.

Cynn, H., Hofmeister, A.M., Burnley, P.C., and Navrotsky, A. (1996) Thermodynamic properties and hydrogen speciation from vibrational spectra of dense hydrous magnesium silicates. Physics and Chemistry of Minerals, 23, 361–376.

Dachs, E., and Geiger. C.A. (2007) Entropies of mixing and subsolidus phase relations of forsterite-fayalite (Mg_2SiO_4-Fe_2SiO_4) solid solution. American Mineralogist, 92, 699–702.

Dorogokupets, P.I., and Oganov, A.R. (2004) Intrinsic anharmoncity in equations of state of solids and minerals. Doklady Earth Sciences, 395, 238–241.

Farmer, V.C., and Lazarev, A.N. (1974) Symmetry and crystal vibrations. In V.C. Farmer, Ed., The Infrared Spectra of Minerals, p. 51–68. Mineralogical Society, London.

Fateley, W.G., Mcdevitt, N.T., and Bentley, F.F. (1971) Infrared and Raman selection rules for lattice vibrations: the correlation method. Applied Spectroscopy, 25, 155–173.

Finkelstein, G.J., Dear, P.K., Jahn, S., Oganov, A.R., Holl, C.M., Meng, Y., and Duffy, T.S. (2014) Phase transitions and equation of state of forsterite to 90 GPa from single-crystal X-ray diffraction and molecular modeling. American Mineralogist, 99, 35–43.

Fridrichová, J., Bačík, P., Illášová, Ľ., Kozáková, P., Škoda, R., Pulišová, Z., and Fiala, A. (2016) Raman and optical spectroscopic investigation of gem-quality smoky quartz crystals. Vibrational Spectroscopy, 85, 71–78.

Gaisler, S.V., and Kolesov, B.A. (2007) Raman spectra of olivine solid solutions $(Fe_xMg_{1-x})_2SiO_4$ and spin-vibration interaction. Journal of Structural Chemistry, 48, 61–65.

Gillet, P., Richet, P., Guyot, F., and Fiquet, G. (1991) High-temperature thermodynamic properties of forsterite. Journal of Geophysical Research, 96, 11805–11816.

Gillet, P., Daniel, I., and Guyot, F. (1997) Anharmonic properties of Mg_2SiO_4-forsterite measured from the volume dependence of the Raman spectrum. European Journal of Mineralogy, 9, 255–262.

Guyot, F., Boyer, H., Madon, M., Velde, B., and Poirier, J.P. (1986) Comparison of the Raman microprobe spectra of $(Mg,Fe)_2SiO_4$ and Mg_2GeO_4 with olivine and spinel structure. Physics and Chemistry of Minerals, 13, 91–95.

Hazen, R.M. (1977) Effects of temperature and pressure on the crystal structure of ferromagesian olivine. American Mineralogist, 62, 286–295.

Hofmeister, A.M. (1987) Single-crystal absorption and reflection infrared spectroscopy of forsterite and fayalite. Physics and Chemistry of Minerals, 14, 499–513.

——— (1997) Infrared reflectance spectra of fayalite, and absorption data from assorted olivines, including pressure and isotope effects. Physics and Chemistry of Minerals, 24, 535–546.

Hohler, V., and Funck, E. (1973) Vibrational spectra of crystals with olivine structure. Zeitschrift Für Naturforschung B, 28, 125–139 (in German).

Holland, T.J.B., and Powell, R. (1998) An internally consistent thermodynamic data set for phases of petrological interest. Journal of Metamorphic Geology, 16, 309–343.

Horita, J., Cole, D.R., Polyakov, V.B., and Driesner, T. (2002) Experimental and theoretical study of pressure effects on hydrogen isotope fraction in the system brucite-water at elevated temperatures. Geochimica et Cosmochimica Acta, 66, 3769–3788.

Hushur, A., Manghnani, M.H., Smyth, J.R., Nestola, F., and Frost, D.J. (2009) Crystal chemistry of hydrous forsterite and its vibrational properties up to 41 GPa. American Mineralogist, 94, 751–760.

Iishi, K. (1978) Lattice dynamics of forsterite. American Mineralogist, 63, 1198–1208.

Isaak, D.G., Anderson, O.L., and Goto, T. (1989) Elasticity of single-crystal forseterite measured to 1700 K. Journal of Geophysical Research, 94, 5895–5906.

Ishibashi, H., Arakawa, M., Yamamoto, J., and Kagi, H. (2012) Precise determination of Mg/Fe ratios applicable to terrestrial olivine samples using Raman spectroscopy. Journal of Raman Spectroscopy, 43, 331–337.

Kieffer, S.W. (1979) Thermodynamics and lattice vibrations of minerals: 3. Lattice dynamics and an approximation for minerals with application to simple substances and framework silicates. Reviews of Geophysics and Space Physics, 17, 35–59.

Klotz, S., Chervin, J.-C., Munsch, P., and Le Marchand, G. (2009) Hydrostatic limits of 11 pressure transmitting media. Journal of Physics D: Applied Physics, 42, 075413.

Kohlstedt, D.L., Keppler, H., and Rubie, D.C. (1996) Solubility of water in the α, β and γ phases of $(Mg,Fe)_2SiO_4$. Contributions to Mineralogy and Petrology, 123, 345–357.

Kolesov, B.A., and Geiger, C.A. (2004) A Raman spectroscopic study of Fe-Mg olivines. Physics and Chemistry of Minerals, 31, 142–154.

Kolesov, B.A., and Tanskaya, J.V. (1996) Raman spectra and cation distribution in the lattice of olivines. Materials Research Bulletin, 31, 1035–1044.

Kroll, H., Kirfel, A., Heinemann, R., and Barbier, B. (2012) Volume thermal expansion and related thermophysical parameters in the Mg,Fe olivine solid-solution series. European Journal of Mineralogy, 24, 935–956.

Lin, C.C. (2003) Pressure-induced metastable phase transition in orthoenstatite $(MgSiO_3)$ at room temperature: A Raman spectroscopic study. Journal of Solid State Chemistry, 174, 403–411.

Liu, L.G., and Mernagh, T.P. (1993) Raman spectra of forsterite and fayalite at high pressures and room temperatures. High Pressure Research, 11, 241–256.

Liu, D., Pang, Y., Ye, Y., Jin, Z., Smyth, J.R., Yang, Y., Zhang, Z., and Wang, Z.

(2019a) In-situ high-temperature vibrational spectra for synthetic and natural clinohumite: Implications for dense hydrous magnesium silicates in subduction zones. American Mineralogist, 104, 53–63.
Liu, D., Wang, S., Smyth, J.R., Zhang, J., Wang, X., Zhu, X., and Ye, Y. (2019b) In situ infrared spectra for hydrous forsterite up to 1243 K: Hydration effect on thermodynamic properties. Minerals, 9, 512.
Manghnani, M.H., Hushur, A., Smyth, J.R., Nestola, F., Dera, P., Sekar, M., Amulele, G., and Frost, D.J. (2013) Compressibility and structural stability of two variably hydrated olivine samples ($Fo_{97}Fa_3$) to 34 GPa by X-ray diffraction and Raman spectroscopy. American Mineralogist, 98, 1972–1979.
McKeown, D.A., Bell, M.I., and Caracas, R. (2010) Theoretical determination of the Raman spectra of single-crystal forsterite (Mg_2SiO_4). American Mineralogist, 95, 980–984.
Michel, R., Ammar, M.R., Poirier, J., and Simon, P. (2013) Phase transformation characterization of olivine subjected to high temperature in air. Ceramics International, 39, 5287–5294.
Motoyama, T., and Matsumoto, T. (1989) The crystal structure and the cation distributions of Mg and Fe of natural olivines. Mineralogical Journal, 14, 338–350.
Mouri, T., and Enami, M. (2008) Raman spectroscopic study of olivine-group minerals. Journal of Mineralogical and Petrological Sciences, 103, 100–104.
Nestola, F., Pasqual, D., Smyth, J.R., Novella, D., Secco, L., Manghnani, M.H., and Dal Negro, A. (2011) New accurate elastic parameters for the forsterite-fayalite solid solution. American Mineralogist, 96, 1742–1747.
Oganov, A.R., and Dorogokupets, P.I. (2003) All-electron and pseudopotential study of MgO: Equation of state, anharmonicity, and stability. Physical Review B, 67, 224110.
——— (2004) Intrinsic anharmonicity in equations of state and thermodynamics of solids. Journal of Physics: Condensed Matter, 16, 1351–1360.
Piriou, B., and McMillan, P. (1983) The high-frequency vibrational spectra of vitreous and crystalline orthosilicates. American Mineralogist, 68, 426–443.
Polyakov, V.B. (1998) On anharomic and pressure corrections to the equilibrium isotopic constants for minerals. Geochimica et Cosmochimica Acta, 62, 3077–3085.
Polyakov, V.B., and Kharlashina, N.N. (1994) Effect of pressure on equilibrium isotope fractionation. Geochimica et Cosmochimica Acta, 58, 4739–4750.
Rao, K.R., Chaplot, S.L., Chowdhury, N., Ghose, S., Hastings, J.M., Corliss, L.M., and Price, D.L. (1988) Lattice dynamics and inelastic neutron scattering from forsterite, Mg_2SiO_4: Phonon dispersion relation, density of states, and specific heat. Physics and Chemistry of Minerals, 16, 83–97.
Redfern, S.A.T., Artioli, G., Rinaldi, R., Henderson, C.M.B., Knight, K.S., and Wood, B.J. (2000) Octahedral cation ordering in olivine at high temperature. II: An in situ neutron powder diffraction study on synthetic $MgFeSiO_4$ (Fa50). Physics and Chemistry of Minerals, 27, 630–637.
Smyth, J.R. (1975) The high temperature crystal chemistry of fayalite. American Mineralogist, 60, 1092–1097.
Smyth, J.R., and Hazen, R.M. (1973) The crystal structures of forsterite and hortonolite at several temperatures up to 900 °C. American Mineralogist, 58, 588–593.
Smyth, J.R., Frost, D.J., Nestola, F., Holl, C.M., and Bromiley, G. (2006) Olivine hydration in the deep upper mantle: Effects of temperature and silica activity. Geophysical Research Letters, 33, L15301.
Suzuki, I., Seya, K., Takei, H., and Sumino, Y. (1981) Thermal expansion of fayalite, Fe_2SiO_4. Physics and Chemistry of Minerals, 7, 60–63.
Wang, S.Y., Sharma, S.K., and Cooney, T.F. (1993) Micro-Raman and infrared spectral study of forsterite under high pressure. American Mineralogist, 78, 469–476.
Wang, C., Jin, Z., Gao, S., Zhang, J., and Zheng, S. (2010) Eclogite-melt/peridotite reaction: Experimental constrains on the destruction mechanism of the North China Craton. Science China Earth Sciences, 53, 797–809.
Wang, X., Ye, Y., Wu, X., Smyth, J.R., Yang, Y., Zhang, Z., and Wang, Z. (2019) High-temperature Raman and FTIR study of aragonite-group carbonates. Physics and Chemistry of Minerals, 46, 51–62.
Wu, Z. (2015) Thermodynamic properties of wadsleyite with anharmonic effect. Earthquake Science, 28, 11–16.
Wu, Z., Huang, F., and Huang, S. (2015) Isotope fractionation induced by phase transformation: First-principles investigation for Mg_2SiO_4. Earth and Planetary Science Letters, 409, 339–347.
Yang, Y., Wang, Z., Smyth, J.R., Liu, J., and Xia, Q. (2015) Water effects on the anharmonic properties of forsterite. American Mineralogist, 100, 2185–2190.
Ye, Y., Shim, S., Prakapenka, V., and Meng, Y. (2018) Equation of state of solid Ne inter-calibrated with the MgO, Au, Pt, NaCl-B2, and ruby pressure scales up to 130 GPa. High Pressure Research, 38, 377–395.
Zha, C.S., Duffy, T.S., Downs, R.T., Mao, H.K., and Hemley, R.J. (1998) Brillouin scattering and X-ray diffraction of San Carlos olivine: Direct pressure determination to 32 GPa. Earth and Planetary Science Letters, 159, 25–33.
Zhu, X., Guo, X., Smyth, J.R., Ye, Y., Wang, X., and Liu, D. (2019) High-temperature vibrational spectra between $Mg(OH)_2$ and $Mg(OD)_2$: Anharmonic contribution to thermodynamics and D/H fractionation for brucite. Journal of Geophysical Research: Solid Earth, 124, 8267–8280.

Manuscript received June 26, 2020
Manuscript accepted November 11, 2020
Manuscript handled by Zhicheng Jing

Endnote:

[1]Deposit item AM-21-107686, Online Materials. Deposit items are free to all readers and found on the MSA website, via the specific issue's Table of Contents (go to http://www.minsocam.org/MSA/AmMin/TOC/2021/Oct2021_data/Oct2021_data.html).